Ultrathin Wetting Layer-Free Plasmonic Gold Films

Robert Lemasters,[†,‡] Cheng Zhang,[*,†,§,∥] Manoj Manjare,[‡] Wenqi Zhu,[§,∥] Junyeob Song,[§,⊥]
Sergei Urazhdin,[‡] Henri J. Lezec,[§] Amit Agrawal,[§,∥] and Hayk Harutyunyan[*,‡]

[‡]Department of Physics, Emory University, Atlanta, Georgia 30322, United States
[§]Physical Measurement Laboratory, National Institute of Standards and Technology, Gaithersburg, Maryland 20899, United States
[∥]Maryland Nanocenter, University of Maryland, College Park, Maryland 20742, United States
[⊥]Department of Electrical and Computer Engineering, Virginia Tech, Blacksburg, Virginia 24061, United States

ABSTRACT: Ultrathin gold films are attractive for plasmonic and metamaterial devices, thanks to their useful optical and optoelectronic properties. However, deposition of ultrathin continuous Au films of a few nanometer thickness is challenging and generally requires wetting layers, resulting in increased optical losses and incompatibility with optoelectronic device requirements. We demonstrate wetting layer-free plasmonic gold films with thicknesses down to 3 nm obtained by deposition on substrates cooled to cryogenic temperatures. We systematically study the effect of substrate temperature on the properties of the deposited Au films and show that substrate cooling suppresses the Volmer–Weber growth mode of Au, promoting early stage formation of continuous Au films with improved surface morphology and enhanced optoelectronic properties. Our results pave the way for straightforward implementation of ultrathin Au-based optoelectronic and plasmonic devices, as well as metamaterials and metasurfaces.

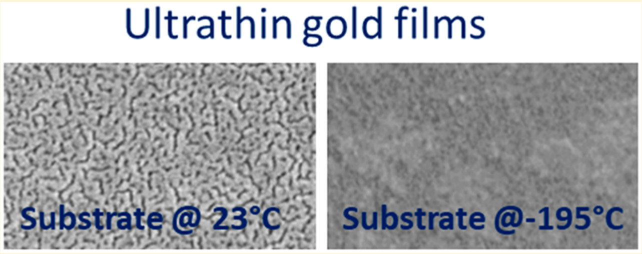

KEYWORDS: *plasmonics, thin films, metamaterials, gold, cryogenic deposition*

Nanoscale thin metal films are essential for the implementation of many nanophotonic and plasmonic devices.[1−6] The most common metals employed for applications in the visible and near-infrared optical range are silver (Ag) and gold (Au), due to their low optical loss. These metals also feature a large negative part of the permittivity in this frequency range, enabling the occurrence of surface plasmon polaritons (SPPs) at their interfaces.[7] Au is significantly more chemically stable than Ag, making it the material of choice for a variety of applications including plasmonic interconnects,[8] modulators,[9] resonators,[10] sensors,[11,12] and metamaterials.[13,14]

In applications utilizing SPPs, optical loss is approximately inversely proportional to the thickness of the metallic layer, because of the scaling of the fraction of the total modal energy localized in the thin metal film. While performance improvement at small film thicknesses comes at a cost of reduced field confinement, the latter is not essential for many applications. For instance, the loss in a long-range SPP waveguide, embedded in free space, is reduced by a factor of 20 when the metal thickness is reduced from 50 to 5 nm, even though the field spillover into free space increases from 300 nm to 1.5 μm for the long-range antisymmetric mode with the free-space wavelength of 780 nm[8] (see Supporting Information, Figure S1). The reduction in loss with thinner metal films is true if only the ohmic losses in an ideal metal slab are considered. In practice, scattering from impurities, defects, or surface roughness become the dominant damping channel in the ultrathin metal film regime.[15]

Thin metallic films are also advantageous for their use as transparent and flexible electrodes in optoelectronic devices such as photovoltaics, diodes and photodetectors.[16−20] Furthermore, they find applications in metal-dielectric heterostructures with hyperbolic or negative index response.[21] In such systems, optical loss diminishes with decreasing thickness of interstitial metal layers. Moreover, using the effective medium approximation is more valid for thin films as they better mimic a homogeneous medium.[22] Finally, as the thickness of the metal layer reaches few monolayers, the resulting strong confinement can lead to the emergence of quantum effects, facilitating fundamentally different plasmonic device functionalities.[23,24]

Fabrication of continuous ultrathin (<10 nm) Au films is challenging, because Au grows in the Volmer–Weber (three-dimensional) mode on common substrates such as fused-silica or silicon.[25] In the initial stage of film growth, the deposited Au atoms cluster together and form isolated islands. As the deposition continues, these isolated islands increase in size, and eventually merge to form a percolated conductive thin Au film. Such a three-dimensional (3D) growth mode leads to a

Received: June 24, 2019
Published: October 3, 2019

minimum thickness value, commonly referred to as the "percolation threshold", below which the deposited Au layer is discontinuous and exhibits a rough surface morphology. The tendency of Au to form clusters has been utilized for the fabrication of low-cost and large-scale plasmonic structures.[26,27]

To reduce the percolation threshold of thin Au films and improve their surface morphology, a thin wetting layer of a different material is generally utilized before Au deposition. Among the common wetting layers are metals such as Ti and Cr,[28] metal oxides such as copper oxide and Al-doped ZnO,[15,29] organic molecules such as mercapto-silane,[30] transition metal dichalcogenides,[31] and polymers.[32] While the wetting layers are effective in reducing the percolation threshold and improving the surface morphology of thin Au films, some wetting materials such as Cr and Ti also introduce additional optical losses and potentially make them incompatible with the devices' functional requirements (see Supporting Information, Figure S2). Furthermore, a recent study shows that an ultrathin Au film with a mass-equivalent thickness as small as 5.4 nm can be prepared using a mercapto-silane wetting layer on fused silica substrate, but due to the interference from this layer, the film's optical transmittance is significantly lower than expected for an ideal Au film of the same mass-equivalent thickness.[30] Finally, wetting layer-free epitaxial growth of crystalline Ag layers has been recently demonstrated on Si substrates with remarkably small thickness and sheet resistivity.[33] However, the need for nontransparent crystalline substrate and complex fabrication method can limit the applications of this method.

The influence of the substrate temperature on the growth of thin metal films is well-known.[17,34−37] Numerous studies have been dedicated to uncover the mechanisms of temperature-dependent growth mechanisms and to find optimal conditions for material deposition. However, most of these studies either have used wetting layers or have metal films deposited on nontransparent substrates such as metals.[38−42] To the best of our knowledge, ultrathin wetting layer-free plasmonic metals on optically transparent substrates, such as fused-silica, have not been reported so far.

Here, we demonstrate that wetting layer-free, ultrathin and plasmonic Au films can be fabricated by deposition directly on fused-silica substrates cooled to cryogenic temperatures. We analyze the effect of substrate temperature on the properties of the deposited ultrathin Au films and find that substrate cooling helps to reduce the mobility of Au atoms on the substrate and thus promotes the formation of ultrathin Au films with improved surface morphology and enhanced optoelectronic characteristics, including lower optical loss and sheet resistance, and higher optical transmittance. We utilize the demonstrated substrate cooling approach to fabricate record-thin, 3 nm thick Au films with good plasmonic properties, that is, large negative real part and small imaginary part of the permittivity. The ultrathin thickness is further verified by the parameter uniqueness test using spectroscopic ellipsometry. Our work establishes a new practical approach for the fabrication of high-quality wetting layer-free ultrathin Au films, paving the way for their applications in optoelectronic and plasmonic devices, as well as metamaterials and metasurfaces.

RESULTS AND DISCUSSION

Deposition of Ultrathin Au Films at Different Temperatures. Ultrathin Au films are deposited on 500 μm thick fused-silica substrates, with substrate temperatures ranging from room temperature (23 °C) down to liquid nitrogen (LN) temperature (−195 °C), using magnetron sputtering in high-vacuum chamber with a base pressure of less than 2.7×10^{-5} Pa. The temperature of the substrate are controlled by attaching the sample holder to a cold finger (Figure 1). To facilitate a good thermal contact between the substrate and cold finger, a 1 mm thick indium layer is inserted between the sample holder and the edge areas of the substrate. This ensures that no indium residue is left on the central part of the substrate, which would have compromised the subsequent optical characterization of the film. To cool the substrate, LN is siphoned into the cold finger reservoir at a rate of ≈400 standard cubic centimeters per minute (sccm). For the lowest temperature used in these experiments, the flow is turned off once the minimum temperature of −195 °C is achieved (as monitored by a thermocouple gauge attached to the sample holder). To consistently achieve intermediate temperatures during deposition, a more involved method was developed. As the LN begins to flow and the temperature begins to drop, the LN flow is turned off well before the target temperature is reached. The substrate temperature continued to drop due to the residual LN in the reservoir. Once the temperature stabilizes, this process is repeated with smaller spurts of LN that are allowed to evaporate until the substrate temperature is stabilized just below the target temperature. The natural warming at the calibrated rate of ≈1 °C/min then results in the increase of the substrate temperature toward the desired value. This process of lowering the temperature just below the target value and allowing it to warm back up to this value is repeated several times to ensure equilibrium between the cold finger and the substrate at the target temperature value.

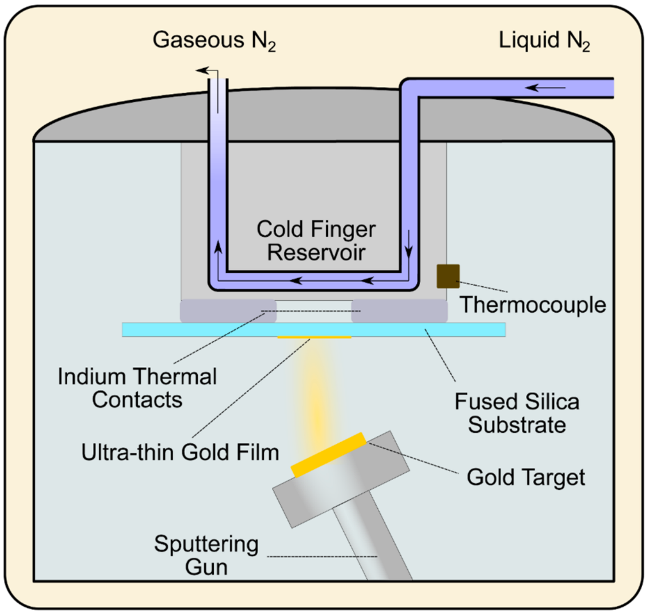

Figure 1. Schematic representation of the deposition chamber and the process for the fabrication of ultrathin Au films.

Table 1. Film Thicknesses Determined by Ellipsometry and Sheet Resistance of the Samples

	$\mathrm{Au}^{5\mathrm{nm}}_{-195\,°\mathrm{C}}$	$\mathrm{Au}^{5\mathrm{nm}}_{-120\,°\mathrm{C}}$	$\mathrm{Au}^{5\mathrm{nm}}_{-80\,°\mathrm{C}}$	$\mathrm{Au}^{5\mathrm{nm}}_{-50\,°\mathrm{C}}$	$\mathrm{Au}^{5\mathrm{nm}}_{-30\,°\mathrm{C}}$	$\mathrm{Au}^{5\mathrm{nm}}_{0\,°\mathrm{C}}$	$\mathrm{Au}^{5\mathrm{nm}}_{23\,°\mathrm{C}}$
best-fit thickness, nm	≈5.66	≈5.06	≈5.09	≈5.47	≈5.85	≈6.32	≈5.64
regression-analysis-fitting MSE	2.742	2.789	5.698	4.706	3.653	6.866	2.765
averaged sheet resistance, Ω/□	15.76	19.77	22.80	23.77	31.37	42.33	70.37

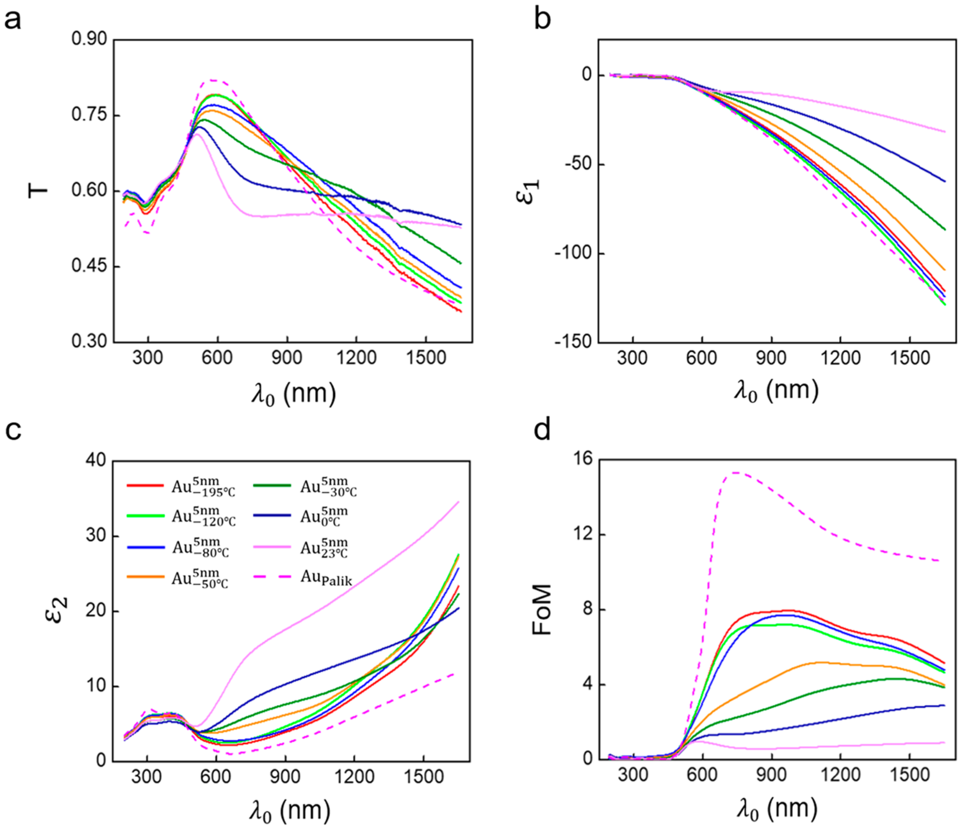

Figure 2. (a) Measured transmittance T vs free-space wavelength λ_0 for samples $\mathrm{Au}^{5\mathrm{nm}}_{-195\,°\mathrm{C}}$, $\mathrm{Au}^{5\mathrm{nm}}_{-120\,°\mathrm{C}}$, $\mathrm{Au}^{5\mathrm{nm}}_{-80\,°\mathrm{C}}$, $\mathrm{Au}^{5\mathrm{nm}}_{-50\,°\mathrm{C}}$, $\mathrm{Au}^{5\mathrm{nm}}_{-30\,°\mathrm{C}}$, $\mathrm{Au}^{5\mathrm{nm}}_{0\,°\mathrm{C}}$, and $\mathrm{Au}^{5\mathrm{nm}}_{23\,°\mathrm{C}}$. The reference ($T = 1$) for all measurements is transmittance through air. The calculated transmittance $T(\lambda_0)$ obtained by transfer matrix method for a 5.66 nm thick Au film on a 500 μm thick fused silica substrate is plotted as well (dashed line). The chosen thickness of 5.66 nm is the same as the measured thickness of sample $\mathrm{Au}^{5\mathrm{nm}}_{-195\,°\mathrm{C}}$ using spectroscopic ellipsometry. The index of Au employed in the calculation is based on ref 43. (b, c) Measured real (b) and imaginary (c) parts of the relative electric permittivity, ε_1 and ε_2, of samples deposited at −195 to 23 °C. The permittivity of Au film from ref 43 is plotted for reference (dashed line). (d) FoM = $|\varepsilon_1(\lambda_0)|/\varepsilon_2(\lambda_0)$ for samples deposited at −195 to 23 °C. The FoM calculated based on the permittivity of Au from ref 43 is plotted for reference (dashed line). Legend of (c) also applies to (a), (b), and (d).

After the substrate reaches the target temperature, the Au deposition is performed in 0.4 Pa of ultrapure argon (Ar), at a rate of 0.5 nm/s determined by a calibrated quartz crystal monitor. The deposited thickness is controlled by the opening time of the mechanical shutter. After the deposition, the sample is kept inside the chamber at the base pressure, until it warmed up to room temperature, to avoid any water vapor condensation or ice crystal formation on the deposited film when exposed to atmosphere. Due to the relatively small difference in the coefficient of thermal expansion of Au and silica substrate and their weak dependence on temperature we do not expect large compressive strain in our samples. Such strain would lead to the "warping" of the film over microscopic regions, which have not been observed even in the samples fabricated at the lowest temperature of −195 °C.

Optoelectronic Characteristics and Surface Morphologies of 5 nm Thick Au. The effect of substrate cooling on the optoelectronic properties and surface morphology of the Au films was studied for 5 nm thick films, deposited on fused-silica substrates at temperatures ranging from the room temperature (23 °C) down to the liquid nitrogen temperature (−195 °C). Seven different temperature values are chosen: 23, 0, −30, −50, −80, −120, and −195 °C. The corresponding Au films are denoted as $\mathrm{Au}^{5\mathrm{nm}}_{23\,°\mathrm{C}}$, $\mathrm{Au}^{5\mathrm{nm}}_{0\,°\mathrm{C}}$, $\mathrm{Au}^{5\mathrm{nm}}_{-30\,°\mathrm{C}}$, $\mathrm{Au}^{5\mathrm{nm}}_{-50\,°\mathrm{C}}$, $\mathrm{Au}^{5\mathrm{nm}}_{-80\,°\mathrm{C}}$, $\mathrm{Au}^{5\mathrm{nm}}_{-120\,°\mathrm{C}}$, and $\mathrm{Au}^{5\mathrm{nm}}_{-195\,°\mathrm{C}}$, respectively.

Spectroscopic ellipsometry is utilized to determine the relative electric permittivity of ultrathin Au samples as a function of free-space wavelength, $\varepsilon_r(\lambda_0) = \varepsilon_1(\lambda_0) + i\varepsilon_2(\lambda_0)$, over the wavelength range from 200 to 1650 nm. To precisely characterize the thin semitransparent absorbing films, the "spectroscopic ellipsometry + transmission (SE + T)" scheme was employed,[44,45] where (*i*) the complex electric field reflection coefficients for *s* and *p* polarizations at three different angles of incidence (55°, 65°, and 75°), and (*ii*) optical transmittance at normal incidence are utilized to extract the complex permittivity and the thickness of the Au layer. In addition, surface morphology of the Au samples was characterized by scanning electron microscopy, and the sheet resistance R_s was measured by the four-point probe method.

The best-fit thickness values along with mean-squared-error (MSE) for different samples determined by spectroscopic ellipsometry are given in Table 1. These values closely match the targeted deposition thickness of 5 nm. The small deviations from this value are likely caused by the fluctuations of the sputtering rate during the deposition of the samples. Similar thickness values are obtained using AFM measurements (see Supporting Information, Figure S3). The measured transmittance spectra (Figure 2a) for the two highest temperature samples $\mathrm{Au}^{5\mathrm{nm}}_{0°\mathrm{C}}$ and $\mathrm{Au}^{5\mathrm{nm}}_{23°\mathrm{C}}$ exhibit a broad dip in the wavelength range of ≈600 to ≈1000 nm. This resonant dip can be attributed to the localized surface plasmon absorption of the Au island-like grains in nonpercolated films (Figure 3a,b). The detrimental effect of such grains on the film's optical properties is also evidenced in the measured permittivity curves of the two films, shown in Figure 2b,c. Here, the real part of the permittivity exhibits less negative values compared to the films deposited at lower temperatures, indicating a degraded metallic property. Similarly, the imaginary part shows the highest values among all the samples over the large portion of the studied spectral range, suggesting an increased optical absorption.

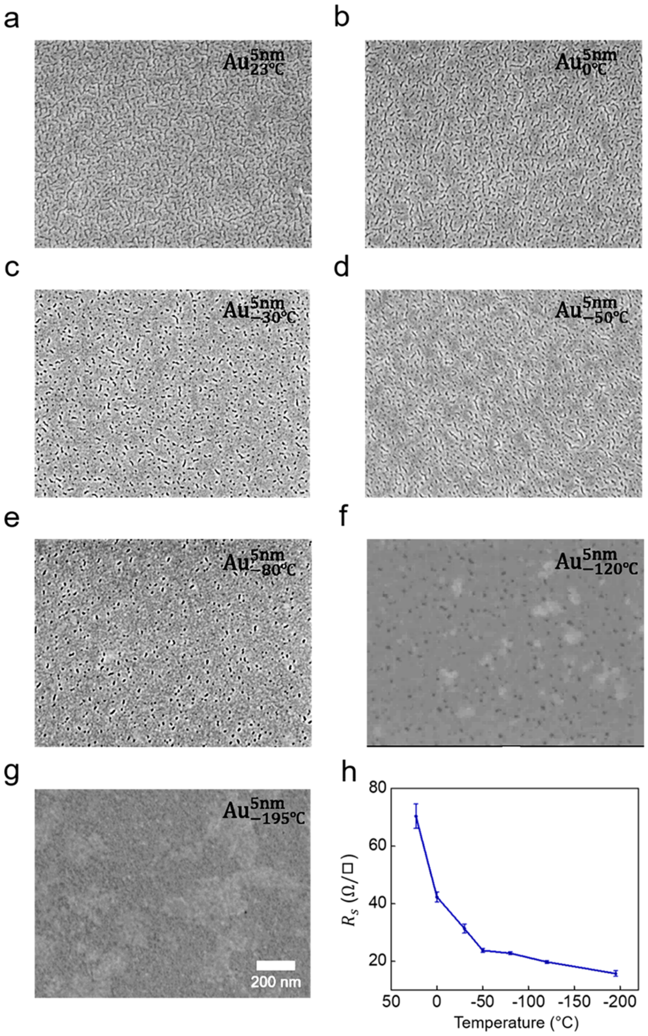

Figure 3. (a−g) Scanning electron micrographs (SEMs) of details of sample $\mathrm{Au}^{5\mathrm{nm}}_{23°\mathrm{C}}$ (a), $\mathrm{Au}^{5\mathrm{nm}}_{0°\mathrm{C}}$ (b), $\mathrm{Au}^{5\mathrm{nm}}_{-30°\mathrm{C}}$ (c), $\mathrm{Au}^{5\mathrm{nm}}_{-50°\mathrm{C}}$ (d), $\mathrm{Au}^{5\mathrm{nm}}_{-80°\mathrm{C}}$ (e), $\mathrm{Au}^{5\mathrm{nm}}_{-120°\mathrm{C}}$ (f), and $\mathrm{Au}^{5\mathrm{nm}}_{-195°\mathrm{C}}$ (g). Scale bar of (g) applies to (a)−(f). (h) Measured sheet resistance of the ultrathin Au film as a function of deposition temperature. Error bars show one standard deviation of the measured data obtained from several consecutive measurements.

For the samples deposited at the reduced substrate temperature, the absorption dip corresponding to the localized surface plasmon resonance gradually diminishes, and transmittance of the film improves, in particular, for the wavelength range from 500 to 800 nm (Figure 2a). It is worth noting that, in these samples, the relatively lower transmittance at longer wavelengths is not due to the increased optical absorption of the film, but rather due to the increased reflection, hinting at improved metallic property of the deposited Au film. Monitoring the surface morphology using SEM imaging also further confirms this picture. Reducing the substrate temperature from $\mathrm{Au}^{5\mathrm{nm}}_{-30°\mathrm{C}}$ to $\mathrm{Au}^{5\mathrm{nm}}_{-120°\mathrm{C}}$ results in gradually reduced void spots on the film, finally leading to a void-free film for the $\mathrm{Au}^{5\mathrm{nm}}_{-195°\mathrm{C}}$ sample (Figure 3c−g). In contrast to the high substrate temperature samples, the measured transmittance curve for $\mathrm{Au}^{5\mathrm{nm}}_{-195°\mathrm{C}}$ does not exhibit localized surface plasmon resonance. Its peak amplitude and spectral shape are in good agreement with the theoretical transmittance spectrum of a continuous, 5.66 nm thick Au film on a fused-silica substrate, calculated using the transfer matrix method (Figure 2a). The thickness of 5.66 nm used in the theoretical transmittance calculations matches the thickness of sample $\mathrm{Au}^{5\mathrm{nm}}_{-195°\mathrm{C}}$, experimentally determined from the spectroscopic ellipsometry. Here, the complex permittivity values for Au used in the calculations (plotted as dashed lines in Figure 2b,c) were taken from a common reference for the permittivity of the bulk Au material.[43] Gradually decreasing the substrate temperature leads to a more negative real part of the permittivity ε_1 (improved metallic properties of the film) and a gradual decrease of the imaginary part ε_2, that is, reduced losses. The figure of merit $\mathrm{FoM} = |\varepsilon_1(\lambda_0)|/\varepsilon_2(\lambda_0)$, which characterizes the quality of the plasmonic film,[46] increases with decreasing deposition temperature over the same wavelength range (Figure 2d). Finally, the improved optoelectronic properties of ultrathin Au films are further evidenced by the measured sheet resistance of the film (Figure 3h), which monotonically decreases as the deposition temperature decreases. The averaged sheet resistance values of the samples are given in Table 1. Aging of the samples are observed over a 6 month period, where the sheet resistance deteriorates by ~30% for samples kept in a nitrogen-purged sample box. The annealing at 120 and 150 °C does not have any significant effects on the sheet resistance of the samples (see Supporting Information, Figure S4). Interestingly, the absence of the wetting layer in our samples does not significantly affect their adhesion to the substrate (see Supporting Information, Figure S5). The optical (permittivity) and electrical (sheet resistance) methods are chosen to characterize the samples since these measurements provide the most technologically relevant information about the averaged optoelectronic properties of our samples. However, to quantitatively study the morphology of the samples, atomic force microscopy (AFM) imaging is performed. The roughness analysis and topographic patterns provided by these measurements are in good agreement with other characterization methods used in this study (see Supporting Information, Figure S6). Namely, root-mean-square (RMS) roughness of the films monotonically increases with the deposition temperature, with $\mathrm{Au}^{5\mathrm{nm}}_{-195°\mathrm{C}}$ exhibiting the smoothest surface.

Based on the results presented above, we conclude that, at the early stages of metal deposition, isolated nanoscopic metal

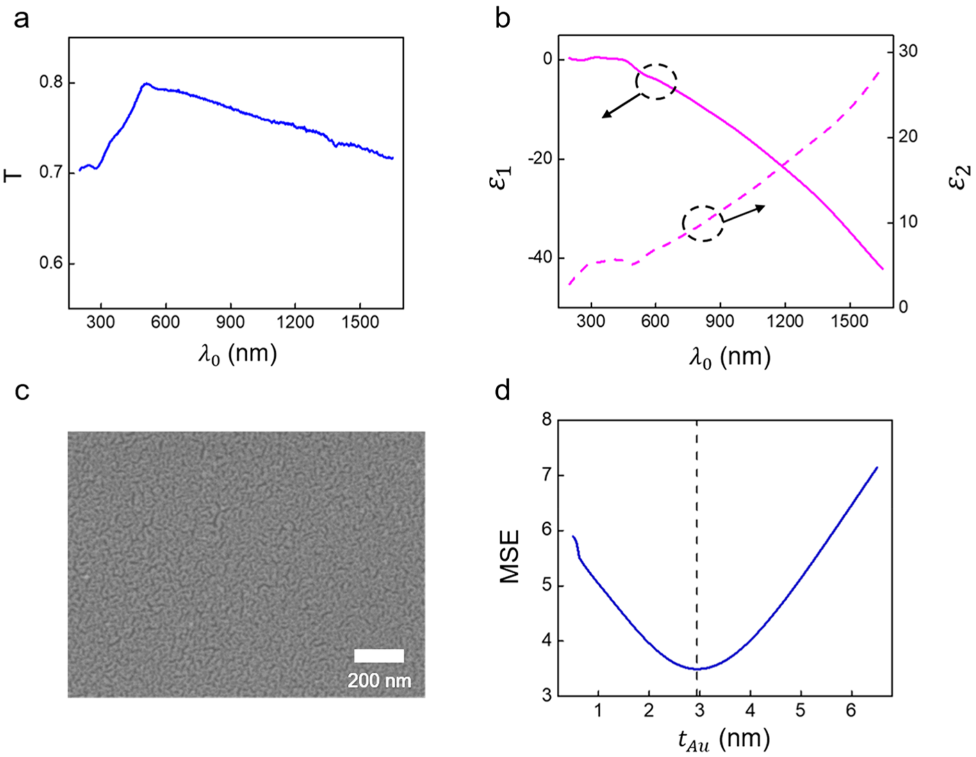

Figure 4. (a) Measured transmittance T vs free-space wavelength λ_0 for sample $\mathrm{Au}^{3\mathrm{nm}}_{-195^\circ\mathrm{C}}$, deposited on a 500 μm thick fused silica substrate. The reference (T = 1) for these measurements is transmittance through air. (b) Measured real (solid line) and imaginary (dashed line) parts of the relative electric permittivity, ε_1 and ε_2, of samples $\mathrm{Au}^{3\mathrm{nm}}_{-195^\circ\mathrm{C}}$. (c) SEM of details of sample $\mathrm{Au}^{3\mathrm{nm}}_{-195^\circ\mathrm{C}}$. (d) Parameter uniqueness test of the thickness of the Au film of sample $\mathrm{Au}^{3\mathrm{nm}}_{-195^\circ\mathrm{C}}$. The dashed line denotes the best-fit thickness value t_{Au} = 2.95 nm.

clusters begin to nucleate and eventually begin to coalesce and increase in size.[17] This is followed by the percolation and, eventually, the formation of a continuous film. The coalescence process of the initial clusters is driven by the minimization of the surface free energy of the system.[47] In this process, smaller clusters with larger relative surface areas diffuse on the surface and coalesce in a "liquid-like" manner into bigger clusters with smaller relative surface areas, lowering the total surface free energy.[48] This makes three-dimensional metal growth thermodynamically more likely than two-dimensional surface growth on the metal−oxide interface, given that the metal−metal cohesion is much stronger than metal−oxide adhesion. Surface quality features are therefore determined by how large the coalescing clusters can get before wetting the surface at the percolation threshold, followed by continuous film formation.[34] If the percolation threshold can be reached sooner, then smaller film features should follow. Cooling down the substrate decreases the diffusion rate of the metal atoms, thus, enabling the formation of stable metal nanoclusters of smaller sizes. This suppresses the 3D clustering and favors the formation of percolated ultrathin metal films. Similarly, faster deposition rates facilitate the formation of continuous films, which is evidenced by a slight improvement of the optical losses (see Supporting Information, Figure S7). To determine the crystalline sizes in our ultrathin films, we have also performed X-ray diffraction (XRD) measurements. The crystalline sizes are estimated from the widths of the X-ray peaks using the Scherrer equation (see Supporting Information, Figure S8). Based on this analysis, it appears that the lower temperature of the substrate results in smaller crystallites, consistent with our diffusion suppression growth picture. However, we must note that the crystalline sizes determined by this method are very close to the 5 nm thickness of the film. Thus, it is plausible that the widths of the peaks are mainly determined by the film thickness.

Plasmonic 3 nm Thick Au Films. Leveraging the beneficial effect of substrate cooling on the formation of ultrathin Au films, as revealed by the study described above, we further explore the possibility of realizing even thinner plasmonic Au films. A nominally 3 nm thick film, $\mathrm{Au}^{3\mathrm{nm}}_{-195^\circ\mathrm{C}}$, is deposited on a fused silica substrate at the liquid nitrogen temperature (deposition rate: 0.5 nm/s) and characterized by spectroscopic ellipsometry, scanning electron microscopy, and four-point probe method.

Compared to the nominally 5 nm thick Au film prepared at the same temperature ($\mathrm{Au}^{5\mathrm{nm}}_{-195^\circ\mathrm{C}}$), sample $\mathrm{Au}^{3\mathrm{nm}}_{-195^\circ\mathrm{C}}$ exhibits a higher transmittance over the spectral range of the measurement (200−1650 nm), thanks to its reduced film thickness (Figure 4a). Meanwhile, it also exhibits degraded relative electric permittivity compared to $\mathrm{Au}^{5\mathrm{nm}}_{-195^\circ\mathrm{C}}$. This is manifested by a smaller negative real part of measured permittivity, ε_1, and a larger positive imaginary part of measured permittivity, ε_2 (Figure 4b). Nevertheless, the measured ε_1 still monotonically decreases beyond 450 nm, confirming the plasmonic behavior of the film. The degraded optical properties could be attributed to the defects remaining from the early stage of the continuous film formation, as evidenced by the void spots in the SEM images (Figure 4c). The averaged sheet resistance is 124.42 Ω/□. The best-fit thickness value determined from spectroscopic ellipsometry is ≈2.95 nm, closely matching the targeted thickness value of 3 nm. The measurements done on samples with 4 nm thickness show that gradual deterioration of the film properties is observed at 3−5 nm thickness range (see Supporting Information, Figure S9).

Finally, we perform a parameter uniqueness test to further verify the achieved record-small thickness of 2.95 nm for a wetting layer-free gold film. During the test, we first choose the thickness of the Au film (t_{Au}) as a test parameter, define a set of 100 test values (evenly spaced between 0.5 and 6.5 nm) around its best-fit value (t_{Au} = 2.95 nm), and then compute the corresponding regression-analysis-fitting MSE in ellipsometry. In the computation, t_{Au} is fixed at each test value, whereas all the other model parameters are allowed to vary, and the resulting MSE (t_{Au}) is recorded. Such a uniqueness test generates a plot of the MSE versus the predefined test parameter values of t_{Au}. As shown in Figure 4d, the curve of MSE (t_{Au}) displays a well-defined minimum around the best-fit value of 2.95 nm. This suggests that the measured film thickness is reliable and uniquely defined, since no other combination of the remaining fit parameters is able to produce a similar MSE for the ellipsometry characterization.

■ CONCLUSION

We systematically studied the effect of substrate temperature on the optoelectronic properties and surface morphology of thin Au films deposited on fused silica. We showed that cooling down the substrate suppresses the Volmer–Weber growth mode of Au, enabling the formation of ultrathin continuous Au films with enhanced optoelectronic properties and improved surface morphologies. Wetting layer-free, plasmonic Au films down to the measured layer thickness of 2.95 nm was achieved by depositing the films on a substrate at the liquid nitrogen temperature. Our work suggests a new approach to the fabrication of wetting layer-free and high-quality ultrathin Au films, which could benefit various Au-based optoelectronic and plasmonic devices, as well as metamaterials and metasurfaces.

■ METHODS

Preparation of Deposition Substrate. Fused-silica substrates were cleaned by sonication in deionized water and detergent, acetone, and isopropyl alcohol sequentially for 20 min at room temperature. The substrates were then dried with nitrogen and transferred into the sputtering chamber.

Spectroscopic Ellipsometry Characterization. The ellipsometry characterization of deposited Au films was performed using a M-2000 ellipsometer (J. A. Woollam Co. Inc.), and data analysis was performed using the CompleteEASE software (J. A. Woollam Co. Inc.). The frequency-dependent permittivity value of each sample was modeled by a combination of Gaussian, Tauc-Lorentz, and Drude oscillators.

SEM, AFM, XRD, and Four-Probe Characterization. The SEM characterization tool used in this study was JEOL 7800F Field Emission Scanning Electron Microscope. AFM imaging was performed on a Bruker Dimension FastScan Atomic Force Microscope. The four-point resistance measurements were done on Four Dimensions 280DI sheet resistance mapping system. Grazing incidence XRD measurements were performed on a Rigaku SmartLab X-ray diffraction system (Copper K-α line at 1.5406 Å). The angle of incidence was 0.7°, scan speed was set as 1°/min, and the scan step was 0.05°.

Sample Disclaimer. Certain commercial equipment, instruments, or materials are identified in this paper in order to specify the experimental procedure adequately. Such identification is not intended to imply recommendation or endorsement by the National Institute of Standards and Technology, nor is it intended to imply that the materials or equipment identified are necessarily the best available for the purpose.

■ ASSOCIATED CONTENT

Ⓢ Supporting Information

The Supporting Information is available free of charge on the ACS Publications website at DOI: 10.1021/acsphotonics.9b00907.

> Simulated mode profiles of long-range surface plasmon polaritons, optical properties of samples with an adhesion layer, film thickness determined by AFM measurements, resistivity measurements assessing the aging and annealing effects, tests assessing the adhesion of the films, AFM measurements of surface roughness for samples deposited at various temperatures, optical properties of samples deposited at different rates, XRD measurement on films deposited at different temperatures, and properties of 4 nm films (PDF)

■ AUTHOR INFORMATION

Corresponding Authors

*E-mail: cheng.zhang@nist.gov.

*E-mail: hayk.harutyunyan@emory.edu.

ORCID

Cheng Zhang: 0000-0002-9739-3511

Hayk Harutyunyan: 0000-0003-0495-746X

Author Contributions

[†]These authors contributed equally to this work.

Notes

The authors declare no competing financial interest.

■ ACKNOWLEDGMENTS

R.L. and H.H. acknowledge support from DoE (DE-SC0020101). C.Z., W.Z., and A.A. acknowledge support under the Cooperative Research Agreement between the University of Maryland and the National Institute of Standards and Technology Center, Award #70NANB14H209, through the University of Maryland. S.U. acknowledges support from NSF (ECCS-1804198 and DMR-1504449). C.Z. acknowledges helpful discussions with Dr. N. Hong.

■ REFERENCES

(1) Meinzer, N.; Barnes, W. L.; Hooper, I. R. Plasmonic meta-atoms and metasurfaces. *Nat. Photonics* **2014**, *8*, 889.

(2) Poddubny, A.; Iorsh, I.; Belov, P.; Kivshar, Y. Hyperbolic metamaterials. *Nat. Photonics* **2013**, *7*, 948.

(3) Genevet, P.; Capasso, F.; Aieta, F.; Khorasaninejad, M.; Devlin, R. Recent advances in planar optics: from plasmonic to dielectric metasurfaces. *Optica* **2017**, *4*, 139–152.

(4) McPeak, K. M.; Jayanti, S. V.; Kress, S. J. P.; Meyer, S.; Iotti, S.; Rossinelli, A.; Norris, D. J. Plasmonic Films Can Easily Be Better: Rules and Recipes. *ACS Photonics* **2015**, *2*, 326–333.

(5) Nagpal, P.; Lindquist, N. C.; Oh, S.-H.; Norris, D. J. Ultrasmooth Patterned Metals for Plasmonics and Metamaterials. *Science* **2009**, *325*, 594–597.

(6) Zhang, C.; Zhao, D.; Gu, D.; Kim, H.; Ling, T.; Wu, Y.-K. R.; Guo, L. J. An Ultrathin, Smooth, and Low-Loss Al-Doped Ag Film and Its Application as a Transparent Electrode in Organic Photovoltaics. *Adv. Mater.* **2014**, *26*, 5696–5701.

(7) Maier, S. A. *Plasmonics: Fundamentals and Applications*; Springer Science and Business Media, 2007.

(8) Berini, P. Long-range surface plasmon polaritons. *Adv. Opt. Photonics* **2009**, *1*, 484–588.

(9) Haffner, C.; Chelladurai, D.; Fedoryshyn, Y.; Josten, A.; Baeuerle, B.; Heni, W.; Watanabe, T.; Cui, T.; Cheng, B.; Saha, S.; Elder, D. L.; Dalton, L. R.; Boltasseva, A.; Shalaev, V. M.; Kinsey, N.; Leuthold, J. Low-loss plasmon-assisted electro-optic modulator. *Nature* **2018**, *556*, 483–486.

(10) Zhu, W.; Xu, T.; Wang, H.; Zhang, C.; Deotare, P. B.; Agrawal, A.; Lezec, H. J. Surface plasmon polariton laser based on a metallic trench Fabry-Perot resonator. *Sci. Adv.* **2017**, *3*, No. e1700909.

(11) Stockman, M. I. Nanoplasmonic sensing and detection. *Science* **2015**, *348*, 287–288.

(12) Mayer, K. M.; Hafner, J. H. Localized Surface Plasmon Resonance Sensors. *Chem. Rev.* **2011**, *111*, 3828–3857.

(13) Yu, N.; Genevet, P.; Kats, M. A.; Aieta, F.; Tetienne, J.-P.; Capasso, F.; Gaburro, Z. Light Propagation with Phase Discontinuities: Generalized Laws of Reflection and Refraction. *Science* **2011**, *334*, 333–337.

(14) Zhang, C.; Pfeiffer, C.; Jang, T.; Ray, V.; Junda, M.; Uprety, P.; Podraza, N.; Grbic, A.; Guo, L. J. Breaking Malus' law: Highly efficient, broadband, and angular robust asymmetric light transmitting metasurface. *Laser Photonics Rev.* **2016**, *10*, 791–798.

(15) Maniyara, R. A.; Rodrigo, D.; Yu, R.; Canet-Ferrer, J.; Ghosh, D. S.; Yongsunthon, R.; Baker, D. E.; Rezikyan, A.; García de Abajo, F. J.; Pruneri, V. Tunable plasmons in ultrathin metal films. *Nat. Photonics* **2019**, *13*, 328–333.

(16) O'Connor, B.; Haughn, C.; An, K.-H.; Pipe, K. P.; Shtein, M. Transparent and conductive electrodes based on unpatterned, thin metal films. *Appl. Phys. Lett.* **2008**, *93*, 223304.

(17) Yun, J. Ultrathin Metal films for Transparent Electrodes of Flexible Optoelectronic Devices. *Adv. Funct. Mater.* **2017**, *27*, 1606641.

(18) Pode, R. B.; Lee, C. J.; Moon, D. G.; Han, J. I. Transparent conducting metal electrode for top emission organic light-emitting devices: Ca–Ag double layer. *Appl. Phys. Lett.* **2004**, *84*, 4614–4616.

(19) Hecht, D. S.; Hu, L.; Irvin, G. Emerging Transparent Electrodes Based on Thin Films of Carbon Nanotubes, Graphene, and Metallic Nanostructures. *Adv. Mater.* **2011**, *23*, 1482–1513.

(20) Zhang, C.; Huang, Q.; Cui, Q.; Ji, C.; Zhang, Z.; Chen, X.; George, T.; Zhao, S.; Guo, L. J. High-Performance Large-Scale Flexible Optoelectronics Using Ultrathin Silver Films with Tunable Properties. *ACS Appl. Mater. Interfaces* **2019**, *11*, 27216–27225.

(21) Smolyaninov, I. I. *Hyperbolic Metamaterials*; Morgan and Claypool Publishers, 2018.

(22) Subramania, G.; Fischer, A. J.; Luk, T. S. Optical properties of metal-dielectric based epsilon near zero metamaterials. *Appl. Phys. Lett.* **2012**, *101*, 241107.

(23) Vidal, G.; Latorre, J. I.; Rico, E.; Kitaev, A. Entanglement in Quantum Critical Phenomena. *Phys. Rev. Lett.* **2003**, *90*, 227902.

(24) Qian, H.; Xiao, Y.; Liu, Z. Giant Kerr response of ultrathin gold films from quantum size effect. *Nat. Commun.* **2016**, *7*, 13153.

(25) Sennett, R. S.; Scott, G. D. The Structure of Evaporated Metal Films and Their Optical Properties. *J. Opt. Soc. Am.* **1950**, *40*, 203–211.

(26) Doron-Mor, I.; Barkay, Z.; Filip-Granit, N.; Vaskevich, A.; Rubinstein, I. Ultrathin Gold Island Films on Silanized Glass. Morphology and Optical Properties. *Chem. Mater.* **2004**, *16*, 3476–3483.

(27) Tesler, A. B.; Chuntonov, L.; Karakouz, T.; Bendikov, T. A.; Haran, G.; Vaskevich, A.; Rubinstein, I. Tunable Localized Plasmon Transducers Prepared by Thermal Dewetting of Percolated Evaporated Gold Films. *J. Phys. Chem. C* **2011**, *115*, 24642–24652.

(28) Todeschini, M.; Bastos da Silva Fanta, A.; Jensen, F.; Wagner, J. B.; Han, A. Influence of Ti and Cr Adhesion Layers on Ultrathin Au Films. *ACS Appl. Mater. Interfaces* **2017**, *9*, 37374–37385.

(29) Xie, J.; Bi, Y.; Ye, M.; Rao, Z.; Shu, L.; Lin, P.; Zeng, X.; Ke, S. Epitaxial ultrathin Au films on transparent mica with oxide wetting layer applied to organic light-emitting devices. *Appl. Phys. Lett.* **2019**, *114*, No. 081902.

(30) Kossoy, A.; Merk, V.; Simakov, D.; Leosson, K.; Kéna-Cohen, S.; Maier, S. A. Optical and Structural Properties of Ultra-thin Gold Films. *Adv. Opt. Mater.* **2015**, *3*, 71–77.

(31) Yakubovsky, D. I.; Stebunov, Y. V.; Kirtaev, R. V.; Ermolaev, G. A.; Mironov, M. S.; Novikov, S. M.; Arsenin, A. V.; Volkov, V. S. Ultrathin and Ultrasmooth Gold Films on Monolayer MoS$_2$. *Adv. Mater. Interfaces* **2019**, *6*, 1900196.

(32) Leosson, K.; Ingason, A. S.; Agnarsson, B.; Kossoy, A.; Olafsson, S.; Gather, M. C. Ultra-thin gold films on transparent polymers. *Nanophotonics* **2013**, *2*, 3.

(33) Abd El-Fattah, Z. M.; Mkhitaryan, V.; Brede, J.; Fernández, L.; Li, C.; Guo, Q.; Ghosh, A.; Echarri, A. R.; Naveh, D.; Xia, F.; Ortega, J. E.; García de Abajo, F. J. Plasmonics in Atomically Thin Crystalline Silver Films. *ACS Nano* **2019**, *13*, 7771–7779.

(34) Campbell, C. T. Ultrathin metal films and particles on oxide surfaces: structural, electronic and chemisorptive properties. *Surf. Sci. Rep.* **1997**, *27*, 1–111.

(35) Kaiser, N. Review of the fundamentals of thin-film growth. *Appl. Opt.* **2002**, *41*, 3053–3060.

(36) Diebold, U.; Pan, J. M.; Madey, T. E. Growth mode of ultrathin copper overlayers on TiO$_2$(110). *Phys. Rev. B: Condens. Matter Mater. Phys.* **1993**, *47*, 3868–3876.

(37) Zhang, T. C.; Mei, Z. X.; Guo, Y.; Xue, Q. K.; Du, X. L. Influence of growth temperature on formation of continuous Ag thin film on ZnO surface by ultra-high vacuum deposition. *J. Phys. D: Appl. Phys.* **2009**, *42*, No. 065303.

(38) Egelhoff, W. F.; Jacob, I. Reflection High-Energy Electron Diffraction (RHEED) Oscillations at 77 K. *Phys. Rev. Lett.* **1989**, *62*, 921–924.

(39) Sergeant, N. P.; Hadipour, A.; Niesen, B.; Cheyns, D.; Heremans, P.; Peumans, P.; Rand, B. P. Design of Transparent Anodes for Resonant Cavity Enhanced Light Harvesting in Organic Solar Cells. *Adv. Mater.* **2012**, *24*, 728–732.

(40) Stefaniuk, T.; Wróbel, P.; Górecka, E.; Szoplik, T. Optimum deposition conditions of ultrasmooth silver nanolayers. *Nanoscale Res. Lett.* **2014**, *9*, 153.

(41) van der Vegt, H. A.; van Pinxteren, H. M.; Lohmeier, M.; Vlieg, E.; Thornton, J. M. C. Surfactant-induced layer-by-layer growth of Ag on Ag(111). *Phys. Rev. Lett.* **1992**, *68*, 3335–3338.

(42) Jing, D.; Ünal, B.; Qin, F.; Yuen, C.; Evans, J. W.; Jenks, C. J.; Sordelet, D. J.; Thiel, P. A. Stranski–Krastanov-like growth of an Ag film on a metallic glass. *Thin Solid Films* **2009**, *517*, 6486–6492.

(43) Lynch, D. W.; Hunter, W. R. Comments on the Optical Constants of Metals and an Introduction to the Data for Several Metals. In *Handbook of Optical Constants of Solids*; Palik, E. D., Ed.; Academic Press: Burlington, 1997; pp 275–367.

(44) Zhang, C.; Hong, N.; Ji, C.; Zhu, W.; Chen, X.; Agrawal, A.; Zhang, Z.; Tiwald, T. E.; Schoeche, S.; Hilfiker, J. N.; Guo, L. J.; Lezec, H. J. Robust Extraction of Hyperbolic Metamaterial Permittivity Using Total Internal Reflection Ellipsometry. *ACS Photonics* **2018**, *5*, 2234–2242.

(45) Secondo, R.; Fomra, D.; Izyumskaya, N.; Avrutin, V.; Hilfiker, J. N.; Martin, A.; Özgür, Ü.; Kinsey, N. Reliable modeling of ultrathin alternative plasmonic materials using spectroscopic ellipsometry. *Opt. Mater. Express* **2019**, *9*, 760–770.

(46) Kinsey, N.; Ferrera, M.; Naik, G. V.; Babicheva, V. E.; Shalaev, V. M.; Boltasseva, A. Experimental demonstration of titanium nitride plasmonic interconnects. *Opt. Express* **2014**, *22*, 12238–12247.

(47) Parker, S. C.; Campbell, C. T. Kinetic model for sintering of supported metal particles with improved size-dependent energetics and applications to Au on TiO$_2$(110). *Phys. Rev. B: Condens. Matter Mater. Phys.* **2007**, *75*, No. 035430.

(48) José-Yacamán, M.; Gutierrez-Wing, C.; Miki, M.; Yang, D. Q.; Piyakis, K. N.; Sacher, E. Surface Diffusion and Coalescence of Mobile Metal Nanoparticles. *J. Phys. Chem. B* **2005**, *109*, 9703–9711.